Sensors & Actuators: B. Chemical 290 (2019) 459–466

Contents lists available at ScienceDirect

Sensors and Actuators B: Chemical

journal homepage: www.elsevier.com/locate/snb

Template-free synthesis of cubic-rhombohedral-In_2O_3 flower for ppb level acetone detection

Fang Chen, Man Yang, Xi Wang, Yang Song, Lanlan Guo, Ning Xie, Xueying Kou, Xiumei Xu, Yanfeng Sun*, Geyu Lu*

State Key Laboratory on Integrated Optoelectronics, College of Electronic Science and Engineering, Jilin University, 2699 Qianjin Street, Changchun 130012, People's Republic of China

ARTICLE INFO

Keywords:
Acetone sensor
Mixed phase
Porous structure
Solvothermal method

ABSTRACT

Analyzing volatile organic compounds in exhaled breath is a noninvasive method that has potential for disease assessment. Herein, acetone sensors based on porous In_2O_3 flowers are synthesized through a facile solvothermal method. Structural characterizations demonstrate that the three-dimensional In_2O_3 flower-like structure comprises porous ultrathin two-dimensional nanosheets. The structural porosity results in a large specific surface area and fast gas diffusion, which can improve the gas sensing performance. The crystalline structure of the prepared hierarchical flower-like In_2O_3 is a mixed phase of rhombohedral and cubic phases according to the XRD patterns. The sensing properties of the cubic-rhombohedral In_2O_3 (bcc-rh-In_2O_3) are also investigated. Compared with commercial-In_2O_3-based sensor, the bcc-rh-In_2O_3 sensor exhibits 2.9 times higher response (Ra/Rg = 12) and shorter response time (ca. 2 s) toward 50 ppm acetone. The bcc-rh-In_2O_3 sensor has a low detection limit of 10 ppb in atmosphere and can easily distinguish acetone from ethanol. The extraordinary properties of the bcc-rh-In_2O_3 sensor are mainly attributed to the n-n heterojunction between rh-In_2O_3 and bcc-In_2O_3.

1. Introduction

Health inspections have gained increasing attention given the continuous improvement of the quality of human life [1–3]. Among available inspection methods, breath analysis is nonintrusive, easy to operate, and fast in obtaining results [4,5]. Gas chromatography can reveal about 3000 volatile organic compounds in human breath; about 200 gases among them are associated with diseases, such as lung cancer, breast cancer, diabetes, and liver disease [6]. Studies have reported that acetone concentration in exhaled air is related to ketone content in blood. The concentration of acetone in breath of healthy individuals should be less than 0.9 ppm, and levels above 1.8 ppm may suggest insulin-dependent diabetic ketosis [7]. A number of scholars have focused on acetone detection. In particular, sensors based on semiconducting metal oxides are of great interest because of their low cost, adjustable performance, and simple device structure [8–10].

The concentrations of most target gases are very low [11]; as such, superior sensing characteristics are required for precise detection. In 2003, Yamazoe et al. [12] reported three key factors in sensor design, namely, receptor function played by the surface of each oxide grain, transducer function played by each grain boundary, and utility factor related to the sensing body. Various strategies have been proposed as follows in accordance with the principles. The first strategy is design of various morphologies, such as nanocubes [13], nanoparticles [14], nanospheres [15], nanoflowers [16], nanotubes [17], nanofibers [18], nanorods [19], inverse opal structures [20], and urchin-like structures [21]. The second strategy is construction of heterostructures. Zhang et al. [22] fabricated In_2O_3/CuO sensors, which exhibited 5 times higher response to ethanol than CuO sensors. The third strategy is doping or loading catalysts. Ma et al. [23] synthesized 0.5 wt% Pt-loaded WO_3 sensor, which shows 5.6 times higher response to CO than the unloaded material.

In_2O_3 is a typical n-type semiconducting metal oxide with a wide band gap and a promising candidate for solar cells [24], touch displays [25], photocatalysts [26], and gas sensors [27] due to its brilliant electrical and optical features. In_2O_3 is a polymorph, i.e., a cubic bixbyite-type In_2O_3 (bcc-In_2O_3, Eg: 2.93 ± 0.15 eV) and a rhombohedral corundum-type In_2O_3 (rh-In_2O_3, Eg: 3.02 ± 0.15 eV) [28–30]. The formation of InOOH is a key step for obtaining rh-In_2O_3, and the presence of $In(OH)_3$ promotes the formation of bcc-In_2O_3 [31,32]. Single-phase In_2O_3 has been fabricated by annealing corresponding precursors. For example, Liu et al. [33] synthesized In_2O_3 octadecahedron

* Corresponding authors.
E-mail addresses: syf@jlu.edu.cn (Y. Sun), lugy@jlu.edu.cn (G. Lu).

https://doi.org/10.1016/j.snb.2019.04.013
Received 27 November 2018; Received in revised form 31 March 2019; Accepted 2 April 2019
Available online 04 April 2019
0925-4005/

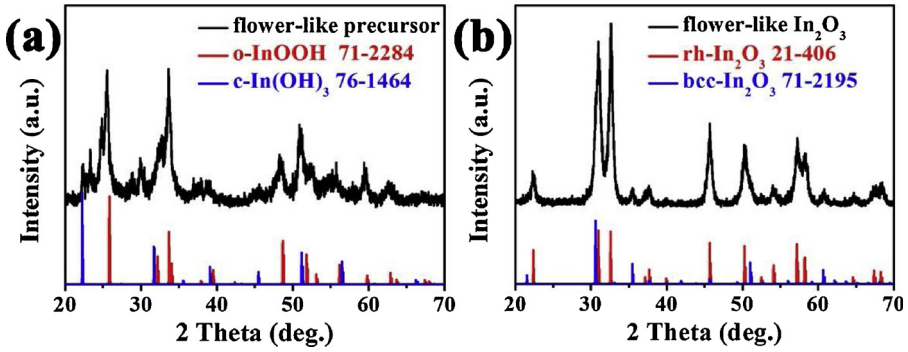

Fig. 1. XRD patterns of the sample: (a) before calcination, (b) after calcination at 400 °C.

by annealing an 18-facet $In(OH)_3$ precursor. Wang et al. [34] synthesized In_2O_3 cubes after annealing $In(OH)_3$ at 500 °C. Singhal et al. [35] prepared rh-In_2O_3 with a rice-grain type morphology by thermal dehydration of InOOH nanostructures. However, compared with bcc-In_2O_3, rh-In_2O_3 has been rarely studied due to its harsh synthesis conditions, such as high temperature and high pressure [36,37]. In previous research, rh-In_2O_3 is mainly used in photoelectric devices [38] and photocatalysts [39]; few reports are available on its use in gas sensors [40]. Moreover, few works have investigated acetone sensors based on mixed-phase flower-like In_2O_3.

In this study, we successfully fabricated hierarchical porous flower-like cubic–rhombohedral In_2O_3 (bcc-rh-In_2O_3) nanostructures through a facial one-step solvothermal route followed by calcination. The sensors based on the as-obtained materials exhibited superior gas sensing properties toward acetone in terms of high response, short response time, low detection limit, and good selectivity. The sensing mechanism was discussed according to the morphology and crystal phase of the sensing materials.

2. Experimental

2.1. Material synthesis

The commercial indium oxide (In_2O_3, 99.995%) was purchased from Nanjing Cinor Chemical Technology Co., Ltd.. Indium nitrate hydrate ($In(NO_3)_3{\cdot}4.5H_2O$, 99.5%) and glycerol ($C_3H_8O_3$, 99%) were obtained from Sinopharm Chemical Reagent Co., Ltd.. Ethanol (C_2H_6O, 99.7%) was purchased from Beijing Chemical Works. All of the chemicals were of analytical reagent grade. Deionized water was used throughout the experiment. The synthesis process of bcc-rh-In_2O_3 is presented as follows.

In brief, bcc-rh-In_2O_3 was prepared by a simple solvothermal route. Firstly, 15 mL of deionized water was mixed with an equal volume of ethanol and stirred on a magnetic stirring plate. Subsequently, 0.3 g of In $(NO_3)_3{\cdot}4.5\ H_2O$ (0.786 mmol) and 8 mL of glycerol were dissolved in the mixture. A Teflon-lined stainless steel autoclave was used as a reaction vessel to hold the reactants. The reaction temperature and time were set as 180 °C and 1 h, respectively. The as-synthesized sediment was collected by centrifugation and purified using deionized water and ethanol solution. The dried sediment was annealed at 400 °C for 2 h to obtain bcc-rh-In_2O_3.

2.2. Material characterization

The crystal structure identification was performed by X-ray diffraction (XRD), using a Rigaku D/Max 2550 X-ray diffractometer with Cu Kα radiation (λ = 1.5418 Å) in the 2θ range of 20-70°. Surface morphologies and microstructures were characterized by scanning electron microscope (SEM, JEOL JSM-7500 F). The transmission electron microscopy (TEM), high-resolution TEM (HRTEM) images were obtained by a JEOL JSM-2100 F transmission electron microscopy. The N_2 adsorption-desorption isotherms were measured by a Micrometrics Gemini VII 2390 analyzer. The surface area data and pore size distribution were obtained by the Brunauer-Emmett-Teller (BET) model and Barrett-Joyner-Halenda (BJH) methods, respectively.

2.3. Fabrication and measurement of gas sensors

The manufacturing and test processes of the sensor were the same as reported previously [41]. An alumina tube was coated with bcc-rh-In_2O_3 slurry. Subsequently, a Ni-Cr alloy coil was inserted into the tube. The tube and the coil were soldered on a plastic base to form a sensor, which was aged in air at 250 °C for more than 2 days. Commercial In_2O_3 powder (99.995%) was purchased from Nanjing Cinor Chemical Technology Co., Ltd. and used to fabricate hand-made sensors for comparison with sensors based on bcc-rh-In_2O_3. The sensor based on commercial In_2O_3 was also fabricated in exactly the same way. Gas sensing performance was evaluated by static testing method. The temperature and humidity of air in atmosphere were approximately 30 °C and 40%RH, respectively. Low concentrations of acetone were obtained from 100 ppm acetone gas, and the other concentrations were obtained from acetone liquid. Response was defined as *Ra/Rg* (reducing gases) and *Rg/Ra* (oxidizing gases), where *Ra* and *Rg* are the resistance of the sensor in air and target gas, respectively. Response and recovery time were defined as the time taken to achieve 90% of the total resistance change.

3. Results and discussion

3.1. Structural and morphological characteristics

The XRD pattern of the sample before calcination is shown in Fig. 1a. Most peaks can be indexed to the orthorhombic phase InOOH (o-InOOH, JCPDS NO. 71-2284) or the cubic phase $In(OH)_3$ (c-$In(OH)_3$, JCPDS NO. 76-1464). Fig. 1b demonstrates the XRD pattern of the as-obtained product after calcination. All of the diffraction peaks can be indexed to the rhombohedral phase In_2O_3 (rh-In_2O_3, JCPDS NO. 21-406) or the cubic phase In_2O_3 (bcc-In_2O_3, JCPDS NO. 71-2195). Hence, the In_2O_3 product is a mixed phase material. Furthermore, the formation mechanism of the mixed phase was investigated.

As early as 2004, Yu et al. [31] reported that the final phase of the In_2O_3 product is greatly affected by the precursor. When the precursor is o-InOOH, the final product is rhombohedral In_2O_3. The c-$In(OH)_3$ precursor is the key to the formation of cubic In_2O_3. Therefore, we infer that the bcc-rh-In_2O_3 mixed phase in the present work was derived from the mixed phase of the precursor. At the reaction temperature (180 °C), the solvents including ethanol (boiling point: 78.3 °C) and deionized water (boiling point: 100 °C) were mostly in the gas state and glycerol (boiling point: 290 °C) was almost in the liquid state. The liquid glycerol acted as the main reactant and combined with In^{3+} to form o-InOOH

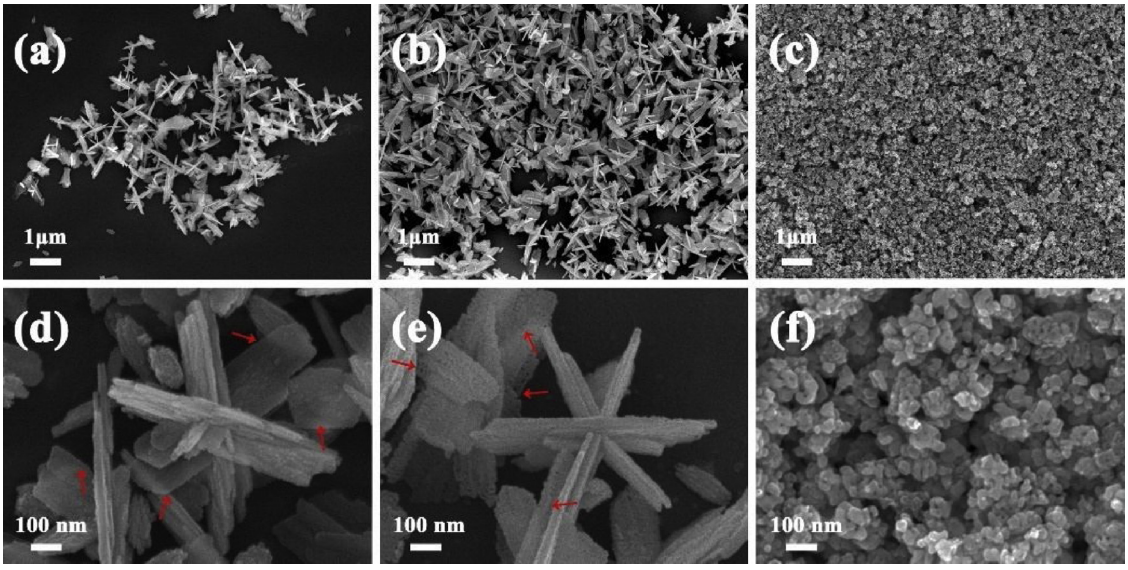

Fig. 2. SEM images of the sample: (a) and (d) before calcination, (b) and (e) after calcination at 400 °C, and (c) and (f) the commercial In_2O_3.

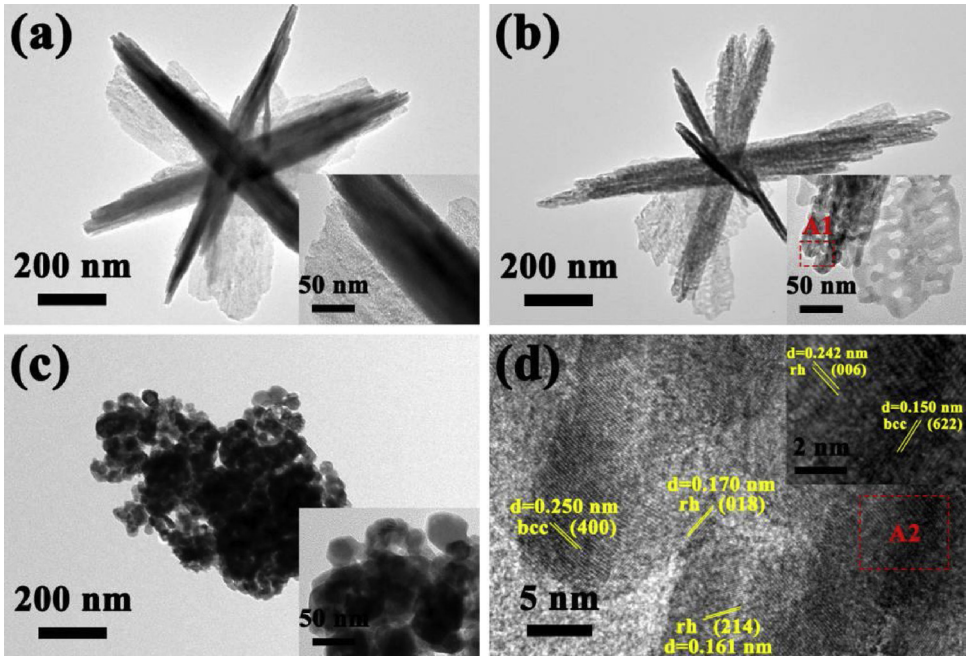

Fig. 3. TEM image of the sample (a) before annealing and (b) after annealing, (c) TEM image of the commercial In_2O_3; the insets in Fig. 3a–c are the high-magnification images; (d) HRTEM image of area A1 in the sample after annealing; the illustration is an enlarged image of area A3.

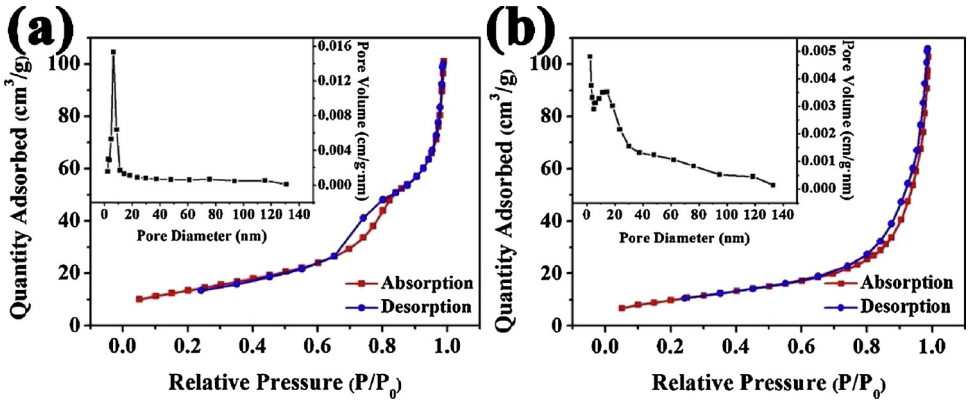

Fig. 4. N_2 adsorption-desorption isotherms of (a) the bcc-rh-In_2O_3 and (b) the commercial In_2O_3; the illustration is the pore size distribution plots.

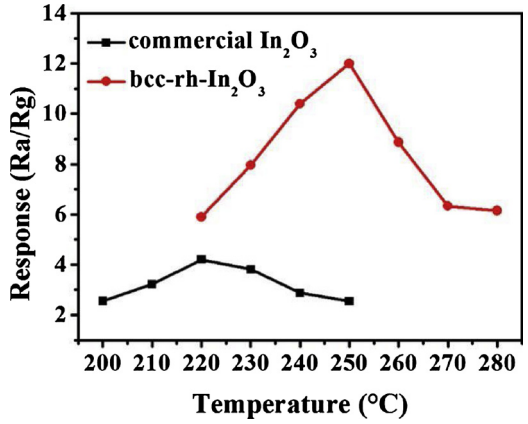

Fig. 5. Responses of sensors based on commercial In_2O_3 and bcc-rh-In_2O_3 to 50 ppm acetone as a function of the operating temperature.

precursor. Given the small amount of liquid water, bcc-$In(OH)_3$ was synthesized.

$$In^{3+} + 3C_3H_8O_3 \rightarrow \text{o-InOOH} + H_2O + 3C_3H_7O_2^{+} \quad (1)$$

$$In^{3+} + 3H_2O \rightarrow \text{bcc-}In(OH)_3 + 3H^{+} \quad (2)$$

Glycerol would form hydrogen bonds with InOOH, contributing to the stabilization and formation of InOOH [42]. A precursor containing o-InOOH and bcc-$In(OH)_3$ was prepared, and the product containing rh-In_2O_3 and bcc-In_2O_3 was obtained after annealing.

$$2\text{InOOH} \rightarrow \text{rh-}In_2O_3 + H_2O\uparrow \quad (3)$$

$$2In(OH)_3 \rightarrow \text{bcc-}In_2O_3 + 3H_2O\uparrow \quad (4)$$

The surface morphology of the sample before calcination is presented in Figs. 2a and d. The precursor possesses a flower-like hierarchical microstructure with a diameter of approximately 1 μm and assembly of several coarse sheets with a high length-to-thickness ratio. As pointed by the arrows in Fig. 2d, some of the sheets are so thin that the other sheets behind them can be seen directly. After calcination, the In_2O_3 product maintained a flower-like morphology with almost the same size as the precursor (Fig. 2b). The nanosheets of the flower are more porous and rougher than the precursor, as indicated by the arrows in Fig. 2e. As shown in Fig. 2c and f, commercial In_2O_3 has irregular grain-like morphology and more agglomerated configurations. Therefore, the sensing film formed by the accumulation of the bcc-rh-In_2O_3 microflowers possesses more gaps and allows the target gas to diffuse into the sensing body more easily than the commercial In_2O_3 sensing film. The porous flower-like hierarchical microstructure might offer abundant frameworks for gas diffusion and benefit gas sensing properties [43].

TEM images reveal that the In_2O_3 flower consists of several nanosheets before and after annealing. The diameter of the flower is about 1 μm, which fits the value estimated from the SEM images. As presented in Fig. 3a and b, the nanosheets become more porous and rougher after calcination. The pores are highly interconnected, providing a channel for the transfer of gas molecules and improving the gas sensing properties. Comparison between the flower-like In_2O_3 and the commercial In_2O_3 indicates that the latter could not disperse well and might be difficult to be fully accessible for the target gas. Fig. 3d shows two crystal phases in the flower. Inter-planar distances of 0.250 and 0.150 nm present a good fit to the (400) and (622) planes of bcc-In_2O_3, respectively. The lattice spacings of 0.161, 0.170, and 0.242 nm are consistent with the (214), (018), and (006) planes of rh-In_2O_3, respectively. The results confirm the existence of a mixed phase, consistent with the XRD pattern.

N_2 adsorption-desorption profiles (Fig. 4) were characterized to clarify the porousness of the samples. Based on the IUPAC classification, the adsorption-desorption isotherms of bcc-rh-In_2O_3 and commercial In_2O_3 can be classified as type IV isotherms. The pore size distribution curve (inset of Fig. 4a and b) was calculated from the desorption branch. The hierarchical In_2O_3 flower displays a narrow pore size distribution centering at approximately 7 nm, implying the formation of a mesoporous structure (2–50 nm) in the sample. The commercial In_2O_3 exhibits a relatively wide pore size distribution centering at approximately 14 nm. In addition, the BET surface areas of the bcc-rh-In_2O_3

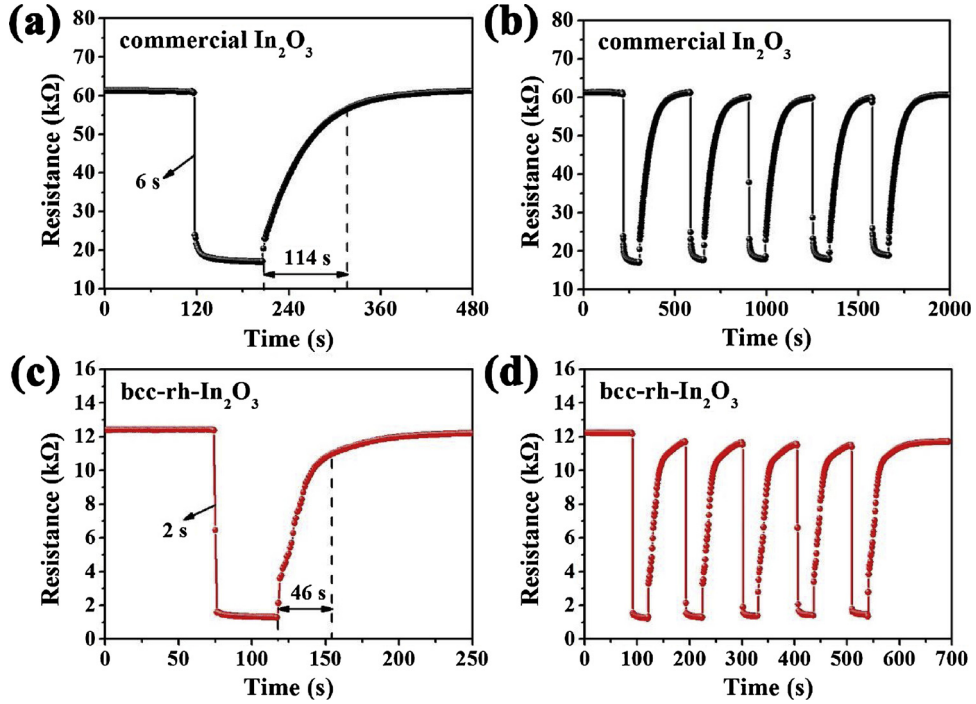

Fig. 6. Dynamic response-recovery curves of the sensor based on (a) commercial In_2O_3 and (b) bcc-rh-In_2O_3 exposed to 50 ppm acetone at their own optimum working temperatures; five reversible cycles of the sensor based on (c) commercial In_2O_3 and (d) bcc-rh-In_2O_3.

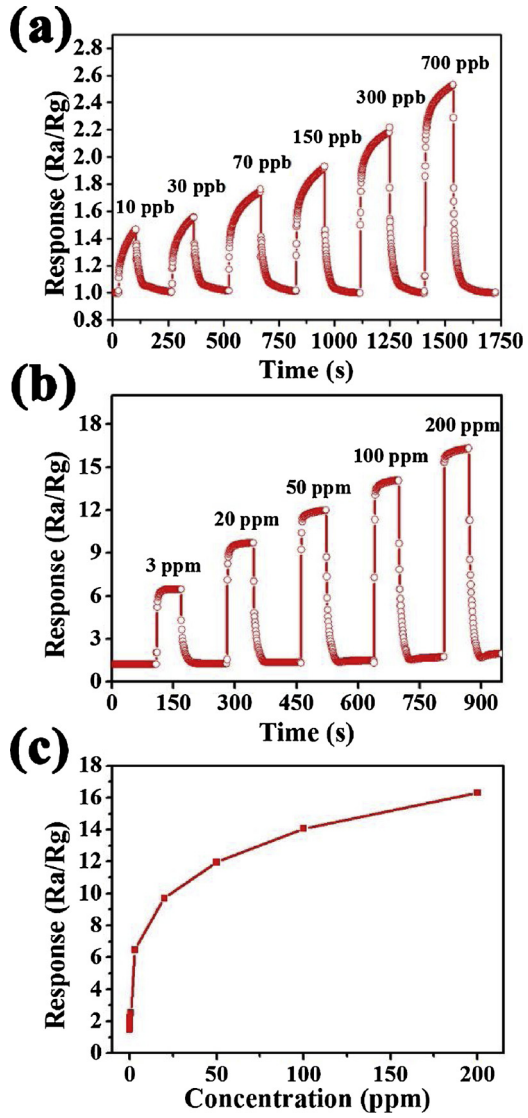

Fig. 7. Time-dependent response curves of the bcc-rh-In_2O_3 sensor to acetone within a range of (a) 10–700 ppb and (b) 3–200 ppm at 250 °C; (c) responses of the bcc-rh-In_2O_3 sensor to 10 ppb-200 ppm acetone at 250 °C.

and the commercial In_2O_3 are 48.6 and 36.7 m^2/g, respectively. The large surface area might contribute to more surface active sites and enhance the sensing properties of the sensors based on bcc-rh-In_2O_3 [44].

3.2. Gas-sensing properties

The surface states of the sensing material are strongly affected by the operating temperature; thus, exploring the optimized working temperature is necessary [45]. In this test and the following experiments, the hand-made sensor fabricated by the commercial In_2O_3 powder was compared with the sensor based on bcc-rh-In_2O_3. As presented in Fig. 5, the responses of these two sensors first increased and then decreased with increasing working temperature. The maximum response of the sensor based on bcc-rh-In_2O_3 reached 12.0 at 250 °C, whereas the sensor based on commercial In_2O_3 achieved the largest response of 4.2 at 220 °C. The optimized working temperatures for further experiments are 250 °C and 220 °C for the sensor based on bcc-rh-In_2O_3 and commercial In_2O_3, respectively.

Fig. 6a and c shows the dynamic response-recovery curves of the sensor based on commercial In_2O_3 and bcc-rh-In_2O_3 to 50 ppm acetone, respectively. The resistance of the sensors, especially the bcc-rh-In_2O_3 sensor dropped quickly as soon as they were exposed to the acetone vapor. Once placed in the air ambient, the resistance recovered to their initial states. The response and recovery time are 2 and 46 s for the bcc-rh-In_2O_3 sensor, and 6 and 114 s for the sensor based on commercial In_2O_3. The test was performed for five cycles, as shown in Fig. 6b and d. The results confirm that both sensors show good stability and reversibility after alternate exposure to air and acetone vapor.

The responses of the bcc-rh-In_2O_3 sensor to low concentrations of acetone (< 1 ppm) and high concentration of acetone (≥ 3 ppm) were tested and plotted in Fig. 7a and b, respectively. The corresponding response increased with increasing acetone concentration, exhibiting typical concentration-dependent response curves. The responses to 10, 30, 70, 150, 300, and 700 ppb acetone are 1.5, 1.6, 1.8, 1.9, 2.2, and 2.5, respectively. The responses to 3, 20, 50, 100, and 200 ppm acetone are 6.5, 9.7, 12.0, 14.1, and 16.3, respectively. Moreover, Fig. 7c shows concentration dependence of bcc-rh-In_2O_3 sensor response. With increasing acetone concentration, the response of the gas sensor increased. When the concentration of acetone is as high as 200 ppm, the bcc-rh-In_2O_3 sensor do not tend to be saturate even though the increasing trend gradually slows down with increasing acetone concentration. Hence, the bcc-rh-In_2O_3 sensor not only has a relatively low detection limit but also a broad detection range. The gas sensing properties of other sensors based on In_2O_3 nanomaterials are listed in Table 1. Compared with the sensors based on In_2O_3 nanomaterials, the fabricated bcc-rh-In_2O_3 sensor displayed the highest response and acceptable recovery time to acetone.

As demonstrated in the radar graph (Fig. 8a), the response plot of the sensor based on commercial In_2O_3 is surrounded by the response plot of the bcc-rh-In_2O_3 sensor, indicating the higher response of the latter for all target gases. In addition, the angle to acetone is sharpest in Fig. 8a, implying high selectivity of the sensor based on bcc-rh-In_2O_3. The responses of the bcc-rh-In_2O_3 sensor to 50 ppm acetone, ethanol, methanol, xylene, formaldehyde, benzene, toluene, carbon monoxide, and ammonia are 12.0, 2.9, 4.8, 3.1, 4.1, 1.4, and 1.2, respectively. In particular, the bcc-rh-In_2O_3 sensor can more clearly distinguish acetone from ethanol compared with the sensors based on SnO_2 nanomaterials [52–55]. The histogram of responses in Fig. 8b verifies that the optimum working temperatures for detection of ethanol and acetone are

Table 1
Comparison of acetone sensing ability of diverse In_2O_3 gas sensors[a].

Material	Temp. (°C)	Conc. (ppm)	Res. (Ra/Rg)	Tres/Trec (s)	Detetion Limit (ppb)	Ref.
In_2O_3microflowers	250	50	13.6	2/46	10	Our work
Inverse opal In_2O_3 microspheres	275	100	13.2	1/51	83.3	[1]
In_2O_3 nanofibers	300	100	6.6	2/32	500	[46]
In_2O_3 hollow microspheres	350	50	11.11	–	500	[47]
In_2O_3 blocks	370	50	9.35	–	–	[48]
Sb-doped In_2O_3 films	200	80	4	–	–	[49]
Au-doped In_2O_3nanofibers	300	100	12.4	2/9	–	[50]
flower-like In_2O_3 microspheres	250	200	9.72	5/182	–	[51]

[a] Temp, temperature; Conc, concentration; Res, response (Ra/Rg); Tres/Trec, response time/recovery time; Detetion Limit, low detection limit; Ref, reference.

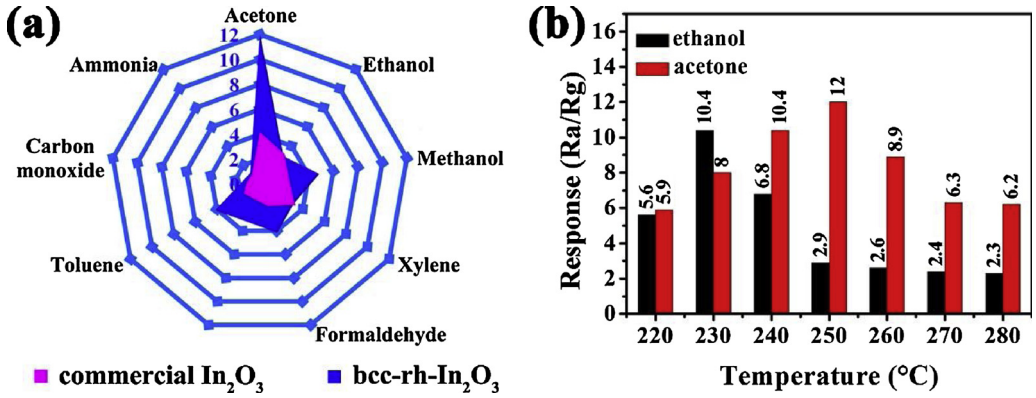

Fig. 8. (a) Responses of the bcc-rh-In_2O_3 sensor and the sensor based on commercial In_2O_3 to 50 ppm various gases at their own optimum working temperatures; (b) Responses of the bcc-rh-In_2O_3 sensor to 50 ppm ethanol and acetone at different working temperatures.

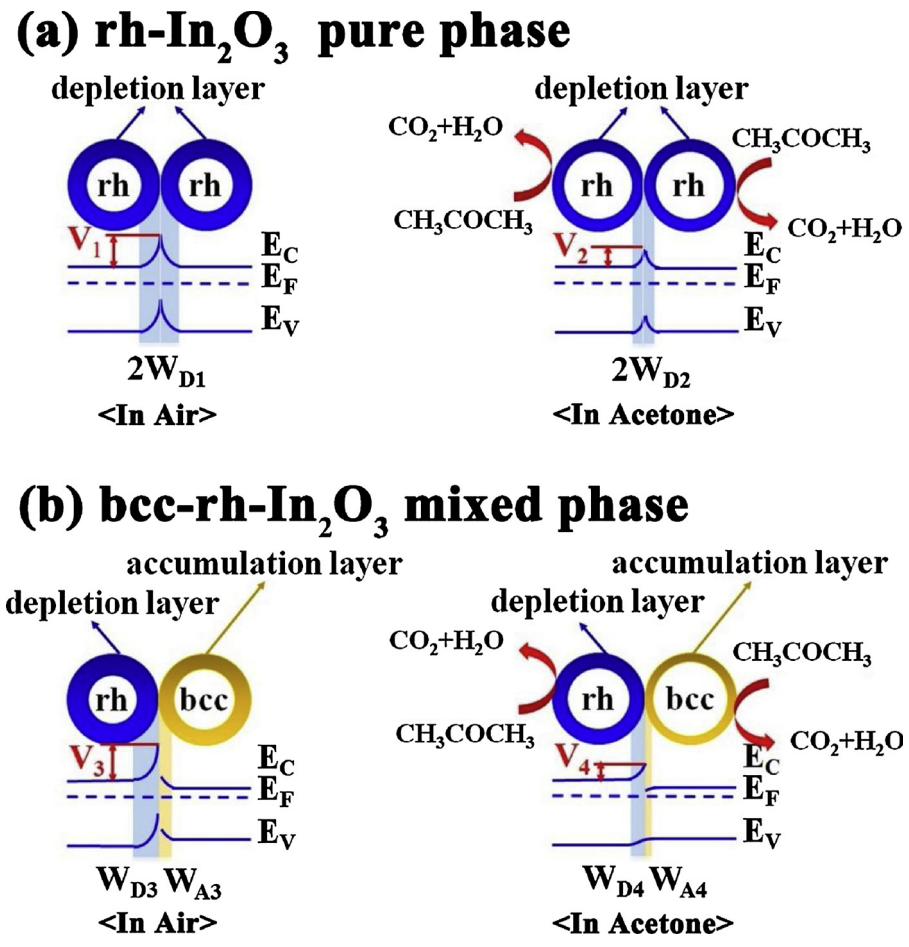

Fig. 9. Energy band diagrams of (a) the rh-In_2O_3 pure phase and (b) the bcc-rh-In_2O_3 mixed phase.

230 °C and 250 °C, respectively. The response to acetone (12.0) is higher than the response to ethanol (10.4) even at their own optimum operating temperatures. At the optimum operating temperature of acetone (250 °C), the response to ethanol decreased from 10.4 to 2.9.

3.3. Gas sensing mechanism

The surface control models and the energy band diagrams of pure rhombohedral phase In_2O_3 are shown in Fig. 9a to provide further insights into the sensing mechanism of the mixed phase In_2O_3. In air, oxygen molecules will be adsorbed on the surface of rh-In_2O_3 and be ionized by capturing electrons from rh-In_2O_3, forming negatively charged oxygen. The adsorption of negatively charged oxygen will result in the formation of an electron depletion layer (W_{D1}) on the surface of rhombohedral In_2O_3 nanoparticles and increase the potential energy barrier (V_1). The specific reactions are as follows:

$$O_2(gas) + 2e^- \rightarrow 2O^-(ads) \quad (5)$$

Once the sensor is exposed to acetone, electrons trapped in the negatively charged oxygen will be released back to In_2O_3 nanoparticles. Thus, the electron depletion layer became narrow ($W_{D2} < W_{D1}$), and the potential energy barrier decreased ($V_2 < V_1$), leading to increased resistance. The chemical reaction equation is as follows:

$$CH_3COCH_3 + 8O^-(ads) \rightarrow 3CO_2 + 3H_2O + 8e^- \quad (6)$$

Furthermore, the energy band diagrams of the mixed phase In_2O_3 are described in Fig. 9b. The work functions of rhombohedral In_2O_3 and cubic In_2O_3 are 4.3 [56] and 5 eV [57,58], respectively. The Fermi level of rh-In_2O_3 is different from that of bcc-In_2O_3. Thus, a typical n–n heterojunction would form when the cubic In_2O_3 nanoparticles come in contact with the rhombohedral In_2O_3 nanoparticles. Moreover, electrons would transfer from rhombohedral In_2O_3 to cubic In_2O_3 until the Fermi levels become consistent because the Fermi level of rh-In_2O_3 is higher than that of bcc-In_2O_3. Therefore, the electron concentration of rh-In_2O_3 is lower than that of pure rhombohedral phase In_2O_3. A wider electron depletion layer ($W_{D3} > W_{D1}$) and a higher potential energy barrier ($V_3 > V_1$) will form on the surface of rh-In_2O_3. Furthermore, the accumulation layer between the rh-In_2O_3 and bcc-In_2O_3 nanoparticles helps the adsorption of oxygen and facilitates the reaction of acetone with the sensing body [22]. Therefore, the gas sensor based on bcc-rh-In_2O_3 nanomaterials can achieve high gas response to the target gases. Besides, flower-like structures can accelerate gas diffusion into the sensor body and enhance the utility factor of the gas sensor. The porous structure of the nanosheets also facilitates the enhancement of the gas sensing characteristics because of the contribution to the high BET area and target gas fluxion in the microflower. Such structure properties also ensure the fast response and recovery speed of the gas sensor [59].

4. Conclusion

In summary, the acetone sensors based on bcc-rh-In_2O_3 flower-like hierarchical structure demonstrate better gas sensing performance compared with those based on commercial In_2O_3. The high response, low detection limit, short response/recovery time, and outstanding selectivity are mainly attributed to the extraordinary N-n heterojunction. The porous and hierarchical structure also contributes to the high response and fast response/recovery speed. Results reveal that the mixed phase In_2O_3 is a good candidate for the fabrication of acetone gas sensors.

Acknowledgement

This work was supported by National Nature Science Foundation of China (Nos. 61573164, 61520106003, 61831011, 61327804).

References

[1] T. Wang, I. Can, S. Zhang, J. He, P. Sun, F. Liu, G. Lu, Self-assembly template driven 3D inverse opal microspheres functionalized with catalyst nanoparticles enabling a highly efficient chemical sensing platform, ACS Appl. Mater. Interfaces 10 (2018) 5835–5844.
[2] F. Huang, W. Yang, F. He, S. Liu, Controlled synthesis of flower-like In_2O_3 microrods and their highly improved selectivity toward ethanol, Sens. Actuators B Chem. 235 (2016) 86–93.
[3] A. Shanmugasundaram, V. Gundimeda, T. Hou, D. Lee, Realizing synergy between In_2O_3 nanocubes and nitrogen-doped reduced graphene oxide: an excellent nanocomposite for the selective and sensitive detection of CO at ambient temperatures, ACS Appl. Mater. Interfaces 9 (2017) 31728–31740.
[4] R. Xing, Q. Li, L. Xia, J. Song, L. Xu, J. Zhang, Y. Xie, H. Song, Au-modified three-dimensional In_2O_3 inverse opals: synthesis and improved performance for acetone sensing toward diagnosis of diabetes, Nanoscale 7 (2015) 13051–13060.
[5] G. Neri, A. Bonavita, G. Micali, N. Donato, Design and development of a breath acetone MOS sensor for ketogenic diets control, IEEE Sens. J. 10 (2010) 131–136.
[6] T. Arakawa, X. Wang, T. Kajiro, K. Miyajima, S. Takeuchi, H. Kudo, K. Yano, K. Mitsubayashi, A direct gaseous ethanol imaging system for analysis of alcohol metabolism from exhaled breath, Sens. Actuators B Chem. 186 (2013) 27–33.
[7] S. Singkammo, A. Wisitsoraat, C. Sriprachuabwong, A. Tuantranont, S. Phanichphant, C. Liewhiran, Electrolytically exfoliated graphene-loaded flame-made Ni-Doped SnO_2 composite film for acetone sensing, ACS Appl. Mater. Interfaces 7 (2015) 3077–3092.
[8] D. Vuong, G. Sakai, K. Shimanoe, N. Yamazoe, Hydrogen sulfide gas sensing properties of thin films derived from SnO_2 sols different in grain size, Sens. Actuators B Chem. 105 (2005) 437–442.
[9] K. Wetchakun, T. Samerjai, N. Tamaekong, C. Liewhiran, C. Siriwong, V. Kruefu, A. Wisitsoraat, A. Tuantranont, S. Phanichphant, Semiconducting metal oxides as sensors for environmentally hazardous gases, Sens. Actuators B Chem. 160 (2011) 580–591.
[10] X. Gao, T. Zhang, An overview: facet-dependent metal oxide semiconductor gas sensors, Sens. Actuators B Chem. 277 (2018) 604–633.
[11] A. Mirzaei, J. Kim, H. Kim, S. Kim, Resistive-based gas sensors for detection of benzene, toluene and xylene (BTX) gases: a review, J. Mater. Chem. C 6 (2018) 4342–4370.
[12] N. Yamazoe, G. Sakai, K. Shimanoe, Oxide semiconductor gas sensors, Catal. Surv. Asia 7 (2003) 63–75.
[13] A. Shanmugasundaram, B. Ramireddy, P. Basak, S. Manorama, S. Srinath, Hierarchical $in(OH)_3$ as a precursor to mesoporous In_2O_3 nanocubes: a facile synthesis route, mechanism of self-assembly, and enhanced sensing response toward hydrogen, J. Phys. Chem. C 118 (2014) 6909–6921.
[14] S. Kim, J. Kim, W. Cheong, I. Lee, H. Lee, H. Im, H. Kong, B. Bae, J. Park, Alcohol gas sensors capable of wireless detection using In_2O_3/Pt nanoparticles and Ag nanowires, Sens. Actuators B Chem. 259 (2018) 825–832.
[15] S. Li, Y. Diao, Z. Yang, J. He, J. Wang, C. Liu, F. Liu, H. Lu, X. Yan, P. Sun, G. Lu, Enhanced room temperature gas sensor based on Au-loaded mesoporous In_2O_3 nanospheres@polyaniline core-shell nanohybrid assembled on flexible PET substrate for NH_3 detection, Sens. Actuators B Chem. 276 (2018) 526–533.
[16] S. Li, P. Lin, L. Zhao, C. Wang, D. Liu, F. Liu, P. Sun, X. Liang, F. Liu, X. Yan, Y. Gao, G. Lu, The room temperature gas sensor based on Polyaniline@flower-like WO_3 nanocomposites and flexible PET substrate for NH_3 detection, Sens. Actuators B Chem. 259 (2018) 505–513.
[17] W. Yang, L. Feng, S. He, L. Liu, S. Liu, Density gradient strategy for preparation of broken In_2O_3 microtubes with remarkably selective detection of triethylamine vapor, ACS Appl. Mater. Interfaces 10 (2018) 27131–27140.
[18] Y. Liu, X. Gao, F. Li, G. Lu, T. Zhang, N. Barsan, Pt-In_2O_3 mesoporous nanofibers with enhanced gas sensing performance towards ppb-level NO_2 at room temperature, Sens. Actuators B Chem. 260 (2018) 927–936.
[19] H. Fu, C. Hou, F. Gu, D. Han, Z. Wang, Facile preparation of rod-like Au/In_2O_3 nanocomposites exhibiting high response to CO at room temperature, Sens. Actuators B Chem. 243 (2017) 516–524.
[20] C. Lee, Z. Dai, D. Kim, H. Li, Y. Jo, B. Kim, H. Byun, I. Hwang, J. Lee, Highly discriminative and sensitive detection of volatile organic compounds for monitoring indoor air quality using pure and Au-loaded 2D In_2O_3 inverse opal thin films, Sens. Actuators B Chem. 273 (2018) 1–8.
[21] M. Ding, N. Xie, C. Wang, X. Kou, H. Zhang, L. Guo, Y. Sun, X. Chuai, Y. Gao, F. Liu, P. Sun, G. Lu, Enhanced NO_2 gas sensing properties by Ag-doped hollow urchin-like In_2O_3 hierarchical nanostructures, Sens. Actuators B Chem. 252 (2017) 418–427.
[22] P. Zhang, H. Zhang, X. Sun, A uniform porous multilayer-junction thin film for enhanced gas-sensing performance, Nanoscale 8 (2016) 1430–1436.
[23] J. Ma, Y. Ren, X. Zhou, L. Liu, Y. Zhu, X. Cheng, P. Xu, X. Li, Y. Deng, D. Zhao, Pt nanoparticles sensitized ordered mesoporous WO_3 semiconductor: gas sensing performance and mechanism study, Adv. Funct. Mater. 28 (2018) 1705268.
[24] T. Koida, Y. Ueno, J. Nishinaga, H. Higuchi, H. Takahashi, M. Iioka, H. Shibata, S. Niki, Cu(In,Ga)Se_2 solar cells with amorphous In_2O_3-based front contact layers, ACS Appl. Mater. Interfaces 9 (2017) 29677–29686.
[25] P. Guo, B. Diroll, W. Huang, L. Zeng, B. Wang, M. Bedzyk, A. Facchetti, T. Marks, R. Chang, R. Schaller, Low-loss near-infrared hyperbolic metamaterials with epitaxial ITO-In_2O_3 multilayers, ACS Photonics 5 (2018) 2000–2007.
[26] D. Ma, J. Shi, Y. Zou, Z. Fan, J. Shi, L. Cheng, D. Sun, Z. Wang, C. Niu, Multiple carrier-transfer pathways in a flower-like In_2S_3/$CdIn_2S_4$/In_2O_3 ternary heterostructure for enhanced photocatalytic hydrogen production, Nanoscale 10 (2018) 7860–7870.
[27] J. Wang, J. Su, H. Chen, X. Zou, G. Li, Oxygen vacancy-rich, Ru-doped In_2O_3 ultrathin nanosheets for efficient detection of xylene at low temperature, J. Mater. Chem. C 6 (2018) 4156–4162.
[28] P. King, T. Veal, F. Fuchs, C. Wang, D. Payne, A. Bourlange, H. Zhang, G. Bell, V. Cimalla, O. Ambacher, R. Egdell, F. Bechstedt, C. McConville, Band gap, electronic structure, and surface electron accumulation of cubic and rhombohedral In_2O_3, Phys. Rev. B 79 (2009) 205211.
[29] M. Wu, C. Wang, Y. Zhao, L. Xiao, C. Zhang, X. Yu, B. Luo, B. Hu, W. Fan, W. Shi, Hydrothermal synthesis of porous rh-In_2O_3 nanostructures with visible-light-driven photocatalytic degradation of tetracycline, Crystengcomm 17 (2015) 2336–2345.
[30] P. Li, H. Fan, Y. Cai, M. Xu, C. Long, M. Li, S. Lei, X. Zou, Phase transformation (cubic to rhombohedral): the effect on the NO_2 sensing performance of Zn-doped flower-like In_2O_3 structures, RSC Adv. 4 (2014) 15161–15170.
[31] D. Yu, D. Wang, Y. Qian, Synthesis of metastable hexagonal In_2O_3 nanocrystals by a precursor-dehydration route under ambient pressure, J. Solid State Chem. 177 (2004) 1230–1234.
[32] C. Chen, D. Chen, X. Jiao, C. Wang, Ultrathin corundum-type In_2O_3 nanotubes derived from orthorhombic InOOH: synthesis and formation mechanism, Chem. Commun. 0 (2006) 4632–4634.
[33] J. Liu, G. Chen, Y. Yu, Y. Wu, M. Zhou, H. Zhang, C. Lv, Y. Zheng, F. He, Controllable synthesis of In_2O_3 octodecahedra exposing {110} facets with enhanced gas sensing performance, RSC Adv. 5 (2015) 44306–44312.
[34] Y. Wang, B. Liu, D. Cai, H. Li, Y. Liu, D. Wang, L. Wang, Q. Li, T. Wang, Room-temperature hydrogen sensor based on grain-boundary controlled Pt decorated In_2O_3 nanocubes, Sens. Actuators B Chem. 201 (2014) 351–359.
[35] A. Singhal, D. Jain, M. Pai, S. Agouram, D. Errandonea, A. Tyagi, Corundum type indium oxide nanostructures: ambient pressure synthesis from InOOH, and optical and photocatalytic properties, RSC Adv. 6 (2016) 108393–108403.
[36] T. de Boer, M. Bekheet, A. Gurlo, R. Riedel, A. Moewes, Band gap and electronic structure of cubic, rhombohedral, and orthorhombic In_2O_3 polymorphs: experiment and theory, Phys. Rev. B 93 (2016) 155205.
[37] B. Garcia-Domene, J. Sans, F. Manjon, S. Ovsyannikov, L. Dubroyinsky,

D. Martinez-Garcia, O. Gomis, D. Errandonea, H. Moutaabbid, Y. Le Godec, H. Ortiz, A. Munoz, P. Rodriguez-Hernandez, C. Popescu, Synthesis and high-pressure study of corundum-type In_2O_3, J. Phys. Chem. C 119 (2015) 29076–29087.
[38] C. Lohaus, C. Steinert, G. Deyu, J. Broetz, W. Jaegermann, A. Klein, Enhancing electrical conductivity of room temperature deposited Sn-doped In_2O_3 thin films by hematite seed layers, Appl. Phys. Lett. 112 (2018) 152105.
[39] S. Lemos, F. Romeiro, L. de Paula, R. Goncalves, A. de Moura, M. Ferrer, E. Longo, A. Patrocinio, R. Lima, Effect of Er^{3+} ions on the phase formation and properties of In_2O_3nanostructures crystallized upon microwave heating, J. Solid State Chem. 249 (2017) 58–63.
[40] L. Gao, F. Ren, Z. Cheng, Y. Zhang, Q. Xiang, J. Xu, Porous corundum-type In_2O_3 nanoflowers: controllable synthesis, enhanced ethanol-sensing properties and response mechanism, CrystEngComm 17 (2015) 3268–3276.
[41] L. Guo, F. Chen, N. Xie, C. Wang, X. Kou, Y. Sun, J. Ma, X. Liang, Y. Gao, G. Lu, Metal-organic frameworks derived tin-doped cobalt oxide yolk-shell nanostructures and their gas sensing properties, J. Colloid Interface Sci. 528 (2018) 53–62.
[42] J. Yin, H. Cao, Synthesis and photocatalytic activity of single-crystalline hollow rh-In_2O_3 nanocrystals, Inorg. Chem. 51 (2012) 6529–6536.
[43] Y. Jeong, W. Koo, J. Jang, D. Kim, M. Kim, I. Kim, Nanoscale PtO_2 catalysts-loaded SnO_2 multichannel nanofibers toward highly sensitive acetone sensor, ACS Appl. Mater. Interfaces 10 (2018) 2016–2025.
[44] X. Li, C. Shao, D. Lu, G. Lu, X. Li, Y. Liu, Octahedral-like CuO/In_2O_3 mesocages with double-shell architectures: rational preparation and application in hydrogen sulfide detection, ACS Appl. Mater. Interfaces 9 (2017) 44632–44640.
[45] X. Fu, J. Liu, Y. Wan, X. Zhang, F. Meng, J. Liu, Preparation of a leaf-like CdS micro-/nanostructure and its enhanced gas-sensing properties for detecting volatile organic compounds, J. Mater. Chem. 22 (2012) 17782–17791.
[46] L. Guo, F. Chen, N. Xie, X. Kou, C. Wang, Y. Sun, F. Liu, X. Liang, Y. Gao, X. Yan, T. Zhang, G. Lu, Ultra-sensitive sensing platform based on Pt-ZnO-In_2O_3 nanofibers for detection of acetone, Sens. Actuators B Chem. 272 (2018) 185–194.
[47] H. Dong, Y. Liu, G. Li, X. Wang, D. Xu, Z. Chen, T. Zhang, J. Wang, L. Zhang, Hierarchically rosette-like In_2O_3 microspheres for volatile organic compounds gas sensors, Sens. Actuators B Chem. 178 (2013) 302–309.
[48] F. Gong, Y. Gong, H. Liu, M. Zhang, Y. Zhang, F. Li, Porous In_2O_3 nanocuboids modified with Pd nanoparticles for chemical sensors, Sens. Actuators B Chem. 223 (2016) 384–391.
[49] N. Pramod, S. Pandey, Influence of Sb doping on the structural, optical, electrical and acetone sensing properties of In_2O_3 thin films, Ceram. Int. 40 (2014) 3461–3468.
[50] F. Li, T. Zhang, X. Gao, R. Wang, B. Li, Coaxial electrospinning heterojunction SnO_2/Au-doped In_2O_3 core-shell nanofibers for acetone gas sensor, Sens. Actuators B Chem. 252 (2017) 822–830.
[51] D. Wei, Z. Huang, L. Wang, X. Chuai, S. Zhang, G. Lu, Hydrothermal synthesis of Ce-doped hierarchical flower-like In2O3 microspheres and their excellent gas-sensing properties, Sens. Actuators B Chem. 255 (2018) 1211–1219.
[52] X. Liu, T. Ma, Y. Xu, L. Sun, L. Zheng, O. Schmidt, J. Zhang, Rolled-up SnO_2 nanomembranes: a new platform for efficient gas sensors, Sens. Actuators B Chem. 264 (2018) 92–99.
[53] X. Kou, N. Xie, F. Chen, T. Wang, L. Guo, C. Wang, Q. Wang, J. Ma, Y. Sun, H. Zhang, G. Lu, Superior acetone gas sensor based on electrospun SnO_2 nanofibers by Rh doping, Sens. Actuators B Chem. 256 (2018) 861–869.
[54] V. Tomer, K. Singh, H. Kaur, M. Shorie, P. Sabherwal, Rapid acetone detection using indium loaded WO_3/SnO_2 nanohybrid sensor, Sens. Actuators B Chem. 253 (2017) 703–713.
[55] Y. Zeng, Y. Wang, L. Qiao, Y. Bing, B. Zou, W. Zheng, Synthesis and the improved sensing properties of hierarchical SnO_2 hollow nanosheets with mesoporous and multilayered interiors, Sens. Actuators B Chem. 222 (2016) 354–361.
[56] H. Jiang, L. Zhao, L. Gai, L. Ma, Y. Ma, M. Li, Hierarchical rh-In_2O_3 crystals derived from InOOH counterparts and their sensitivity to ammonia gas, CrystEngComm 15 (2013) 7003–7009.
[57] Y. Wang, Y. Li, K. Yu, Z. Zhu, Controllable synthesis and field emission enhancement of Al_2O_3 coated In_2O_3 core-shell nanostructures, J. Phys. D Appl. Phys. 44 (2011) 105301.
[58] B. Wang, X. Jin, Z. Ouyang, Synthesis, characterization and cathodoluminescence of self-assembled 1D ZnO/In_2O_3 nano-heterostructures, CrystEngComm 14 (2012) 6888–6903.
[59] J. Lee, Gas sensors using hierarchical and hollow oxide nanostructures: overview, Sens. Actuators B Chem. 140 (2009) 319–336.

Fang Chen: received her B. Eng. degree from the Electronics Science and Engineering department, Jilin University, China in 2017. Her work is the synthesis and characterization of the semiconducting functional materials and gas sensors.

Man Yang: received the BS degree in Changchun University of Science and Technology in 2018. She is currently studying for his MS degree in College of Electronic Science and Engineering, Jilin University, China.

Xi Wang: entered her MS course from department of Physical Chemistry, Jilin University, China, in 2016. Now, she is studying for her PhD degree, engaged in the synthesis and characterization of the semiconducting functional materials and gas sensors.

Yang Song: received his B. Eng. degree from the Electronics Science and Engineering department, Jilin University, China in 2017. His work is the synthesis and characterization of the semiconducting functional materials and gas sensors.

Lanlan Guo: entered her MS course from department of Inorganic Chemistry, Jilin University, China, in 2014. Now, she is studying for her PhD degree, engaged in the synthesis and characterization of the semiconducting functional materials and gas sensors.

Ning Xie: received his B. Eng. degree from the Electronics Science and Engineering department, Jilin University, China in 2016. His work is the synthesis and characterization of the semiconducting functional materials and gas sensors.

Xueying Kou: received the B. Eng. degree in department of electronic sciences and technology in 2015. She is currently studying for her M.E. Sci. degree in College of Electronic Science and Engineering, Jilin University, China. Now, she is engaged in the synthesis and characterization of the semiconducting functional materials and gas sensors.

Xiumei Xu: received her PhD degree from Jilin University of China in 2014. Now, she is an associate professor in Nanyang Normal University. She is engaged in the synthesis and characterization of the semiconducting functional materials and gas sensors.

Yanfeng Sun: obtained his PhD from Jilin University of China in 2007. Presently, he is a professor in Electronics Science and Engineering department of Jilin University. His current research interests are nanoscience and gas sensors.

Geyu Lu: received the BS degree in electronic sciences in 1985 and the MS degree in 1988 from Jilin University in China and the Dr Eng degree in 1998 from Kyushu University in Japan. Now he is a professor of Jilin University, China. Now, he is interested in the development of functional materials and chemical sensors.